PHYSICAL REVIEW B **107**, 184107 (2023)

Local structure of solid and liquid Au as a function of temperature by x-ray absorption spectroscopy

Nodoka Hara,[1] Georghii Tchoudinov,[1] Adriano Filipponi,[2] and Andrea Di Cicco[1]
[1]*Physics Division, School of Science and Technology, Università di Camerino, 62032 Camerino, Italy*
[2]*Dipartimento di Scienze Fisiche e Chimiche, Università degli Studi dell'Aquila, Via Vetoio, 67100 L'Aquila, Italy*

(Received 28 November 2022; accepted 25 April 2023; published 15 May 2023)

Accurate Au L-edge EXAFS (extended x-ray absorption fine structure) spectra of elemental Au have been collected and analyzed in a wide range of temperatures from 80 to 1400 K in the solid and liquid phases. Suitable samples for high-temperature measurements in the liquid phase were obtained by *in situ* reduction of an organic precursor. The data analysis was carried out using reliable multiple-scattering calculations including relativistic corrections (GnXAS), especially important for this heavy element. Simultaneous L_1-, L_2-, and L_3-edge refinements were performed and local structural results were compared with those obtained in previous studies based mainly on x-ray diffraction experiments. In the solid phase, an increased asymmetry of the first-neighbor distribution is observed for increasing temperatures while the average distance is found to be compatible with present thermal expansion data. The structure refinement of liquid Au was carried out considering the short-range contribution to the pair distribution function $g(r)$, using available x-ray diffraction data as a constraint for long-range order. We have shown that EXAFS is extremely sensitive to the local structure and that the $g(r)$ of liquid Au is characterized by a clear shift of the foot of the $g(r)$ and a slight shortening of the position of the maximum as compared with the previous data. The present data put to a test advanced computer simulations based on embedded atom models.

DOI: 10.1103/PhysRevB.107.184107

I. INTRODUCTION

Gold, with $Z = 79$ and electronic configuration [Xe]$4f^{14}5d^{10}6s^1$, is a noble metal (i.e., highly resistant to oxidation or corrosion) with the larger mass within group 11 elements. Owing to the *sd* character of the conduction band it is often regarded as a transition metal. Its importance through several millennia of human history and civilizations cannot be neglected, but still nowadays gold deserves a strong scientific interest both in fundamental research and applications. Gold condensed phases continue to attract considerable attention. In the high-pressure domain, recent advances were achieved by shock-wave [1,2] and diffraction experiments [3] aimed at the phase diagram and melting curve determination. Ultrafast experiments were able to probe melting dynamics in the ps timescale [4]. In addition, the possibility to produce a number of nanostructures including clusters [5], nanoribbons [6], and nanopourus structures [7] make such an element very interesting for applied research.

Gold represented a theoretical challenge for the accurate prediction of electron affinity and ionization potential [8]. The theoretical prediction of structure and dynamical properties of gold at ambient pressure in the solid and liquid phases was a traditional field of research where a number of optimized interaction potentials were developed and applied, including tight binding models [9], embedded atom method (EAM) [10,11], or bond order models [12]. First-principles calculations were also exploited to predict the high-pressure phase diagram [13] or structure and dynamical properties [14].

The availability of an optimized interatomic potential model, possibly of the EAM type, able to accurately predict the experimental behavior in a wide range of thermodynamic conditions has been one of the focus of the cited research. Apart from a number of crystallographic properties the ability of the potential to reproduce the radial distribution function of the liquid state was often cited in the literature (Ref. [9] Fig. 8, Ref. [10] Figs. 5, 6, 7, and Ref. [11] Fig. 12). Considering that the most critical part of the potential is the pair repulsive core [10] it can be understood that the comparison with structural techniques able to provide information on the rising foot of the atomic distributions for a wide range of thermodynamic conditions is very useful. The only existing diffraction experiment in the liquid state was performed by Waseda and Othani back in 1974 [15,16]. Present knowledge on the temperature evolution of the ambient pressure crystalline phase structure is also obtained by x-ray diffraction (see Ref. [17] and references therein). Owing to the onset of long-range order the type of information obtained by diffraction on crystals is quite different from the radial distribution function obtained in the liquid case.

Another experimental technique suitable to investigate the local structure around selected absorbing sites is the extended x-ray absorption fine structure (EXAFS or simply XAFS) [18]. One main advantage is that it can be applied indifferently to crystalline or disordered matter such as liquid or amorphous systems (see, for example, Ref. [19]) obtaining essentially the same information. In this work, we present the analysis of high-quality multiple L_1, L_2 and L_3-edge XAFS measurements on elemental bulk gold, performed using synchrotron radiation in a wide temperature range both in the solid and liquid phases, with the purpose to provide independent profiles for the radial distribution function in liquid and crystalline Au. The temperature evolution of the first-neighbor distribution shape poses severe bounds to the potential models and may be useful for future theoretical research in this fields. Modern XAFS data-analysis methods are based on spectra simulations by means of multiple scattering (MS) theory [18,20] within the Muffin tin (MT) approximation, in which the electronic charge densities and potentials of each scattering site are spherically averaged. Due to the high kinetic energy of photoelectrons in the EXAFS region, the MT approximation is sufficiently accurate to describe the potential. In a previous work [21], the importance of relativistic effects in the XAFS of Au has been highlighted using the GNXAS package [20,22], which is a software for XAFS structure analysis based on MS calculations, including a new scheme of relativistic corrections for the scattering t-matrix [21,23]. In this work, we took advantage of present advances in the GNXAS data-analysis method [20] which offers the possibility of multiple-edge refinements [24] and proper account of relativistic effects [21,23]. Moreover GNXAS is suitable for reliable refinements of the local liquid structure as described in previous publications (see Refs. [19,25] and references therein), using the available $g(r)$ data obtained by diffraction techniques as a constraint for the medium and long-range ordering. In this study, we refined the structure of crystalline Au as a function of temperature from 80 to 1300 K and of liquid Au at 1400 K (the melting point of Au is 1337 K [17]) using Au L-edge XAFS. There are presently few previous works dealing with the XAFS analysis of the local structure of crystalline gold (see Refs. [26,27] and references therein) and no data at high temperatures both in the solid and liquid phase.

This paper is organized as follows. In Sec. II, we report the experimental details for sample preparation and collection of Au L-edge XAFS data as a function of temperature; in Sec. III, we discuss the details of the XAFS data analysis, the results obtained for crystalline Au in a wide temperature range from 80 to 1300 K, and the determination of the local structure of liquid Au at 1400 K by XAFS; Sec. V is devoted to the conclusions.

II. EXPERIMENTAL DETAILS

The data subject to the present analysis were collected in a dedicated run at the D42 beamline of the Laboratoire pour l'utilisation du rayonnement électromagnétique (LURE, Orsay France) back in 1994 and never previously analyzed or published. The beamline, exploiting the bending magnet emission of the positron storage ring DCI, operating at 1.85 GeV with typical 320 mA injection currents and long lifetime, was equipped with a Si (311) channel-cut monochromator and two ionization chambers to monitor the incoming I_0 and transmitted intensity I_1 of the x-ray beam. The chambers were filled with Ar-air mixtures optimized to achieve the best signal-to-noise ratio for bulk samples in transmission geometry, in a way to absorb (at ≈12 keV) about 30% of the beam in I_0 and most of the transmitted beam in I_1. Between the two ion chambers we introduced the glass vessel of our (at the time) newly developed furnace [28] equipped with two glued polyimide (Kapton) windows. The top flange of the furnace was equipped with two electrical feedthroughs connected to a folded graphite resistive heater suitable to host the sample pellet. An additional feedthrough was used to house a K thermocouple with the junction inserted in the graphite pocket and used to monitor the sample temperature. After sample loading the vessel was evacuated with a turbo pump. The sample was processed *in situ* and successively measured in thermodynamic equilibrium conditions. The reliability of such historical facilities and experimental strategies make the data presented in this paper still representative of the best achievable quality for bulk samples measurements at high temperatures.

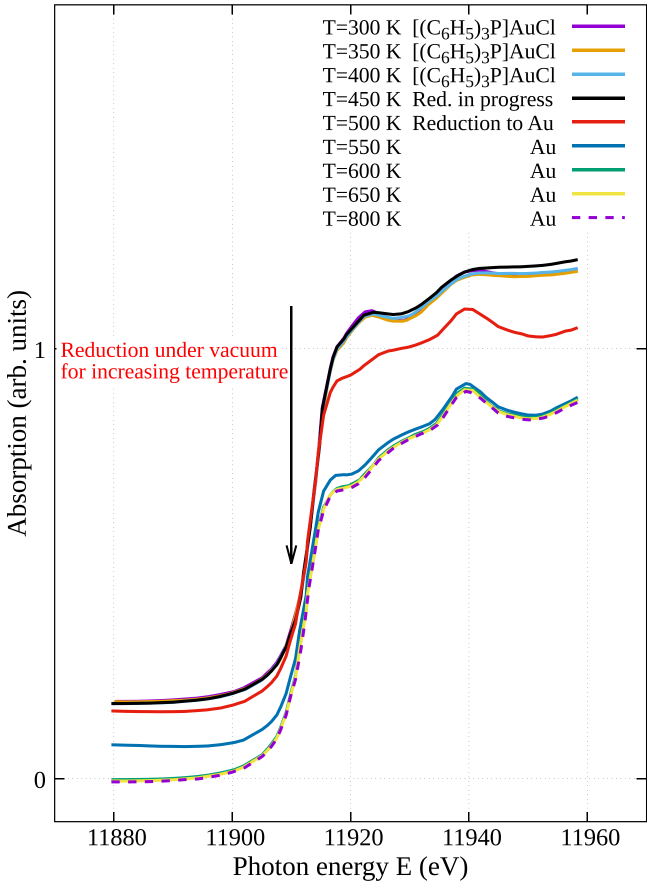

FIG. 1. Reduction process of [$(C_6H_5)_3$P]AuCl precursor powders dispersed in BN, observed *in situ* by measuring the Au L_3-edge spectra for increasing temperatures. In the 480–540 K temperature range, XAS spectra display Au reduction and coalescence into metallic particles indicating the precursor decomposition in fine Au particles. Final XAFS spectra were equivalent to those of Au thin foils.

Gold samples optimized for x-ray absorption spectroscopy experiments in a wide temperature range were prepared by mixing boron nitride (BN) high purity powder with Chloro(triphenylphosphine)gold(I) [$(C_6H_5)_3$P]AuCl precursor powder in a 8:1 mass ratio. All chemicals were commercial with nominal purity >99.9%. The micrometric powder mixture was inserted into a 13 mm inner diameter pellet die and pressed to about 7 ton to obtain compact self-standing sample disks. The disks were filed into rectangular shapes and loaded in the furnace vessel. When the system was under high-vacuum conditions the sample was processed to turn the precursor compound grains into a dispersion of (sub)-micrometric Au crystalline particles embedded in the BN pellet matrix. The sample was progressively heated while monitoring *in situ* the x-ray absorption near edge structure (XANES) evolution at the Au L_3-edge, as illustrated in Fig. 1. In the initial scans the $[(C_6H_5)_3P]AuCl$ precursor spectrum can be identified. In the temperature range 500–550 K, the spectra display Au reduction and coalescence into metallic particles indicating the precursor decomposition. In successive scans at higher temperatures, it is possible to follow the absorption decrease associated with the vaporization of the organic component. After recovering high-vacuum conditions, the sample was heated up to above the melting point to stabilize the gold particles shapes.

By considering that Au is about 2/5 of the molecular weight of the precursor compound and that Au bulk density is about 10 times greater than that of $[(C_6H_5)_3P]AuCl$, the partial Au density increases by a factor 25 in the reduction/coalescence process. Correspondingly the grain diameter is reduced by a factor of about $25^{\frac{1}{3}} \simeq 3$. This means that precursor grains with size in the 1–3 μm range become Au spherical particles with diameters in the 0.3–1 μm range, still representative of bulk specimens. Such a dispersion is mechanically stable through the Au melting and is sufficiently fine grained to provide a homogeneous Au effective thickness along the sample cross-section (see Ref. [29]).

X-ray absorption fine structure (XAFS) spectra were collected at the L_3, L_2, and L_1 edges in a wide energy range. The solid phase was measured at the temperatures 300, 500, 700, 900, 1100, and 1300 K acquiring two spectra with a total integration time of 4 s per point. Five spectra in the liquid phase were collected at 1400 K with a total integration time of 10 s per point. The 300 K L-edge spectra of the Au grain dispersion resulted identical (within the noise) with reference spectra collected on a 5-μm-thick Au foil sample measured at 300 and 80 K using a liquid nitrogen cryostat.

III. XAFS DATA ANALYSIS

A. Method

The data analysis has been performed using the GNXAS package [20,22,24]. Multiple-Scattering (MS) calculations have been performed following standard procedures. We used the structure of face-centered-cubic (fcc) gold at room temperature (lattice parameter $a = 4.081$ Å [21]) as a model for MS simulations. Muffin-tin radii have been generated using the Norman criterion and a complex Hedin-Lundqvist potential has been chosen to account for energy-dependent exchange effects and inelastic losses. Phase shift calculations for the photoabsorbing (excited) and neutral Au atoms have been performed using the relativistic correction introduced in PHAGEN [21], for the L_1, L_2 and L_3 edges of Au. In phase-shift calculations, we have neglected possible thermal effects for the negligible dependence of t matrices (scattering amplitudes related to the phase shifts) upon slight changes of the interatomic distances (thermal expansion).

As usual in GNXAS data analysis, the scattering matrices have been used to build up the irreducible MS signals related to the fcc gold structure relevant for the final XAFS data-analysis refinement of the L_1, L_2, and L_3 edges (see also [21]). Those irreducible signals are two-body and three-body MS terms up to the fourth shell: $\gamma_1^{(2)}$ (first-shell irreducible two-body signal); $\gamma_1^{(3)}$ (irreducible three-body signal corresponding to an equilateral triangle); $\eta_2^{(3)}$, $\eta_3^{(3)}$, and $\eta_4^{(3)}$ (sum of the two- and three-body signals of the long bond configuration and the triangular configuration at respectively 90°, 120°, and 180°). For liquid Au, reference $\gamma^{(2)}$ signals have been calculated for the first-neighbor distances. In addition, the total $\gamma^{(2)}$ contribution associated with long-range distances was calculated following procedures described elsewhere [19] [tail of the pair distribution $g(r)$].

Refinements of XAFS experimental data of solid systems require to take into account thermal (and in some cases static) disorder. Indeed XAFS probes the average of MS signals associated with the corresponding ensemble of instantaneous atomic positions (see, for example, Refs. [18,22] and references therein). This can be accomplished assuming a suitable model for thermal broadening around an average configuration. A standard Gaussian model can work at sufficiently low temperatures, but at high temperature, an-harmonic effects may be present as widely discussed elsewhere (see, for example, Refs. [25,30,31]). For two-body signals, the bond-length distribution may be conveniently modeled using a Γ-like function

$$p(r) = \frac{2N}{\sigma|\beta|\Gamma(\frac{4}{\beta^2})}\left[4\beta^{-2} + \frac{2(r-R)}{\beta\sigma}\right]^{\left(\frac{4}{\beta^2}-1\right)} \times \exp\left[-\frac{4}{\beta^2} - \frac{2(r-R)}{\beta\sigma}\right] \tag{1}$$

successfully used in several crystalline systems accounting for moderate deviations from a simple Gaussian shape. It should be noted that this approach is equivalent to the cumulant expansion method but at variance with the latter accounts for the entire cumulant series associated with the specific model. The parameters appearing in Eq. (1) have an obvious structural meaning: N is the coordination number; R is the average distance; σ^2 is the distance variance (the so-called Debye-Waller factor); β is the dimensionless skewness parameter; $\Gamma(x)$ is the Euler Gamma function. In particular, the β parameter, which is related to the third cumulant by $\beta = \frac{C_3}{\sigma^3}$, measures the deviation from the Gaussian (harmonic, $\beta = 0$) limit and is particularly interesting in the present data analysis for increasing thermal vibrations. The Γ-like function [Eq. (1)] can be also successfully used for modeling the main peak of the pair distribution in liquids [19].

An important aspect of the XAFS data analysis is the atomic background that for the Au L-edges is particularly complex, being affected by the presence of multielectron channels involving $4f$ and $4d$ electrons (at respectively 110 and 370 eV above the L edges) as reported in Ref. [32]. The relative size of these additional features increases as the amplitude of the XAFS signal decreases at high temperatures, requiring to introduce additional steplike functions in the

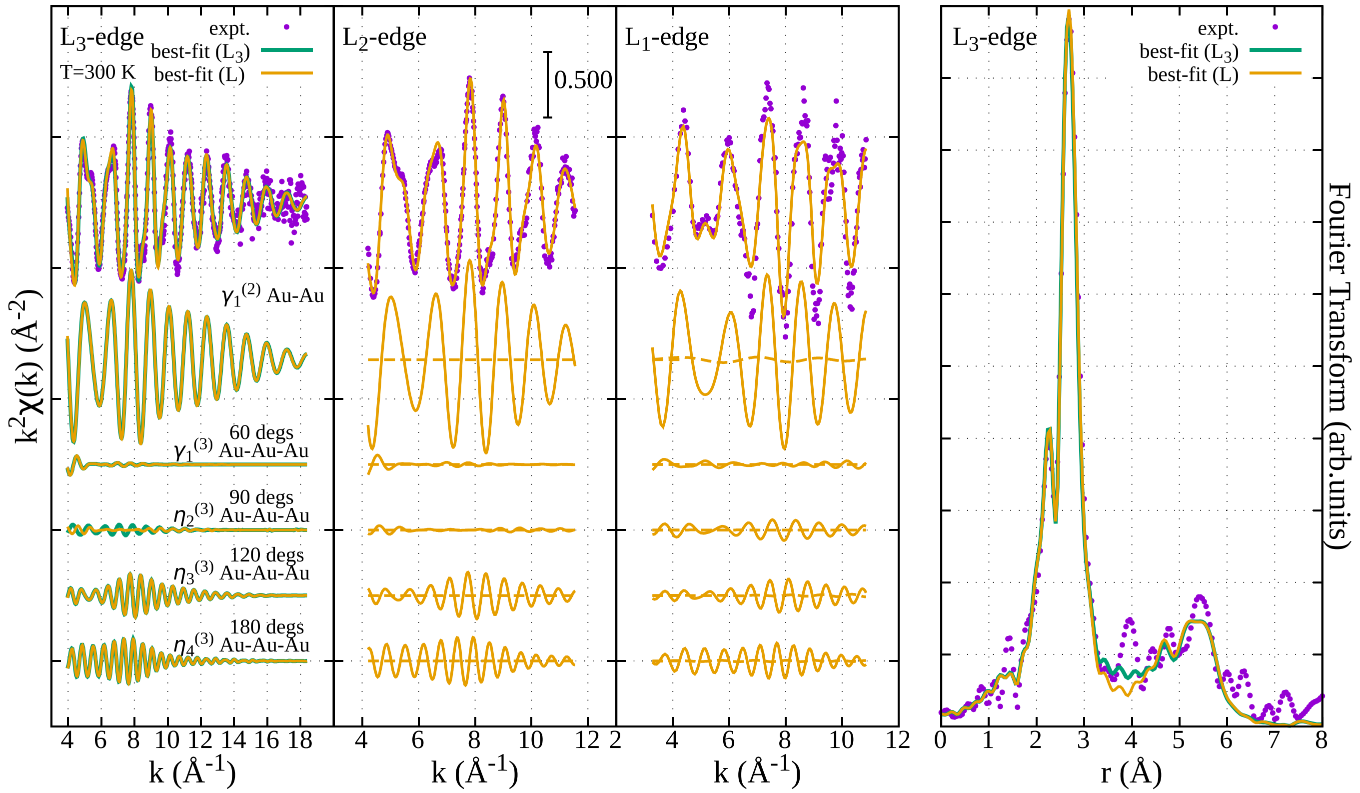

FIG. 2. (Left, upper curves) L_3, L_2, and L_1 edges experimental XAFS data of crystalline gold at 300 K (purple dots) compared with the results of the best-fit refinements (L_3 edge only in green, multiple-edge in orange). (Left, lower curves) Individual two-body Au-Au and three-body Au-Au-Au contributions as described in the text. Continuations of the signal of previous edges are reported as dashed lines. (Right) Fourier transform (FT) of L_3-edge XAFS experimental (purple dots) and L_3 (green) or multiple-edge (orange) best-fit calculations at 300 K.

modeling of the atomic background as illustrated in previous works [32,33].

The XAFS structural refinement was thus performed using standard procedures within the GNXAS programs. The difference between the raw XAFS experimental data and the model including the MS simulations [22] was minimized in the space of the structural, nonstructural and background parameters using the FITHEO program. The refinement has been first performed for powder crystalline gold (c-Au) at 300 K, checking that the results were compatible within the errors with those of the c-Au foil. It has to be noticed that XAFS nonstructural empirical parameters (namely the amplitude reduction factor S_0^2 and the difference between the experimental and theoretical energy scales E_0) of the subsequent higher temperature fitting have been first calibrated on the XAFS spectrum at room temperature, in order to minimize fluctuations of the correlated parameters. Single and multiple (simultaneous) L-edge structural refinements in the entire temperature range were carried out verifying the accuracy of the structural results by evaluating the error bars on selected parameters. Contour maps were also produced for highly correlated parameters like those affecting the signal frequency (E_0 and R).

B. Solid Au

In Fig. 2, we report, as an example, the series of L-edge XAFS $k^2\chi(k)$ experimental spectra (purple dots) of c-Au at 300 K compared with the present best-fit MS refinements (green lines for L_3-edge fit, orange lines for a multiple L-edge fit including the L_3, L_2, and L_1 spectra). The quality of the refinement is extremely good for all the L edges under consideration and the difference between L_3 and multiple L-edge refinement falls within the experimental noise. In this particular case of multiple-edge refinement of a monoatomic system, the addition of L_2- and L_1-edge XAFS is simply increasing the statistics for measuring the same observables (the Au two-body and three-body distributions) but it is also showing the accuracy of the present MS simulations. As outlined above, MS signals with two and three body contributions up to the fourth shell corresponding to $\gamma_1^{(2)}$, $\gamma_1^{(3)}$, $\eta_2^{(3)}$, $\eta_3^{(3)}$, and $\eta_4^{(3)}$ signals were used for the XAFS data analysis of solid c-Au in the 80–1300 K temperature range.

The individual irreducible MS signals related to the two and three-body configurations are also displayed for each XAFS spectrum and clearly the strongest contribution is related to the first neighbors as also shown by the main peak of the XAFS Fourier transform reported in the right-hand panel of Fig. 2

The same data-analysis strategy has been applied to the entire set of c-Au XAFS data collected at different temperatures. In Fig. 3, we compare the c-Au L_3-edge $\chi(k)$ experimental data and their Fourier transforms with the best-fit results at 80, 300, 500, 700, 900, 1100, and 1300 K, respectively. The agreement between experiments and simulations is excellent in the whole range of temperatures.

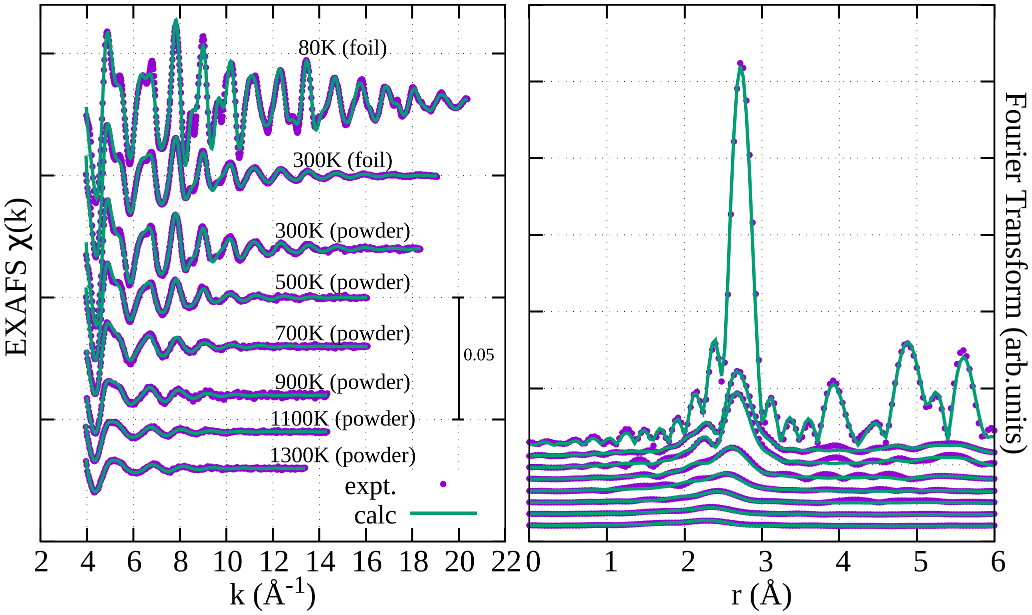

FIG. 3. Experimental L_3 XAFS data of solid c-Au at 80, 300, 500, 700, 900, 1100, and 1300 K (purple dots) compared with best-fit MS simulations (green line) obtained using the GNXAS package with scalar relativistic approximation for the phase shifts. Best-fit refinements were obtained considering two- and three-body contributions up to the fourth shell.

The main structural parameters defining the first-neighbor distribution in c-Au are listed in Table I and shown in Fig. 4. No significant difference between L_3-edge and multiple L-edge refinements were found and we report the latter. Looking at Fig. 4, we can notice that the best-fit structural parameter compare really well with estimates obtained by x-ray diffraction (XRD) and simple models (lines; for more details, see Sec. IV). For increasing temperatures, thermal expansion occur and the average interatomic distance follows this trend (left panel of Fig. 4). The mean square relative displacement or bond variance σ_R^2 is also increasing with temperature slightly departing from a simple Einstein model at high temperatures (middle panel of Fig. 4). The bond variance is well below the uncorrelated limit $2u^2$ at low temperatures but correlation is decreased at higher temperatures. Moreover, the asymmetry of the distribution (monitored by β) increases at high temperatures as also predicted by estimates of the trend of the third cumulant C_3 [39] ($\beta = \frac{C_3}{\sigma^3}$, right panel of Fig. 4). For completeness, we mention our results for relevant XAFS nonstructural parameters such as the amplitude reduction factors S_0^2 and the difference between the experimental and theoretical energy scales E_0 for each L edge under consideration. Those parameters are usually correlated with those of the local structure like R, σ_R^2, and β. We have found $S_0^2 = 0.78(2)$, 0.88(3), and 0.85(2) for L_3, L_2 and L_1 edges, respectively, at all temperatures under consideration. The uncertainty in S_0^2 values at different temperatures is mainly related to small fluctuations in the normalization at edge energy (edge jump). The E_0 energy has been found to be a few eV above the experimental edge energy E_E calculated at the first inflection point [$E_0 - E_E(L_3) = 7.7(8)$ eV, $E_0 - E_E(L_2) = 6(1)$ eV, and $E_0 - E_E(L_1) = 2.8(8)$ eV] with small fluctuations (less than 1 eV) as a function of the temperature.

TABLE I. Best-fit first-neighbor parameters resulting from present XAFS refinements of crystalline Au at various temperatures. The columns report from left to right: sample type (Au foil or powder dispersion), measured temperature T (typical uncertainty ∼1%), average distance R, bond variance σ^2 and skewness β (errors in brackets on the last significant digits). All results are obtained from multiple L-edge refinements, except those of the 5-μm-thick foil at 300 K for which we measured only the L_3-edge XAFS.

Sample	T (K)	R (Å)	σ^2 (10^{-3} Å^2)	β
foil	80	2.876(2)	2.7(2)	0.15(2)
	300[a]	2.886(3)	9.3(2)	0.36(4)
powder	300	2.886(3)	9.1(2)	0.35(4)
	500	2.897(3)	15.2(3)	0.44(4)
	700	2.906(5)	22.6(6)	0.49(4)
	900	2.918(7)	32(1)	0.63(5)
	1100	2.931(4)	43(2)	0.70(3)
	1300	2.941(4)	52(3)	0.72(3)

[a] L_3 edge data.

Statistical errors on structural parameters were evaluated using standard techniques within GNXAS taking into account the noise on the XAFS experimental data. Contour maps among relevant parameters showing correlations were produced using the CONTOUR program. Typical contour maps for c-Au L_3 edge XAFS at 300 K are shown in Fig. 5 as an example of evaluating uncertainty on the structure parameters. The 95% confidence level corresponds to the first ellipse in those plots. A contour map considering R, the first-shell distance, and $E_0^{L_3}$, the L_3-edge energy, is shown in the left panel of Fig. 5. In this case, the statistical error 2σ for the first-neighbor distance R is found to be ±0.003 Å and for L_3 edge energy E_0 is found to be ±0.4 eV. In the right panel of Fig. 5, a contour map considering the R and β first-neighbor parameters is shown. The statistical error of β is determined to be within ±0.04. As shown by the ellipsoid contour shapes

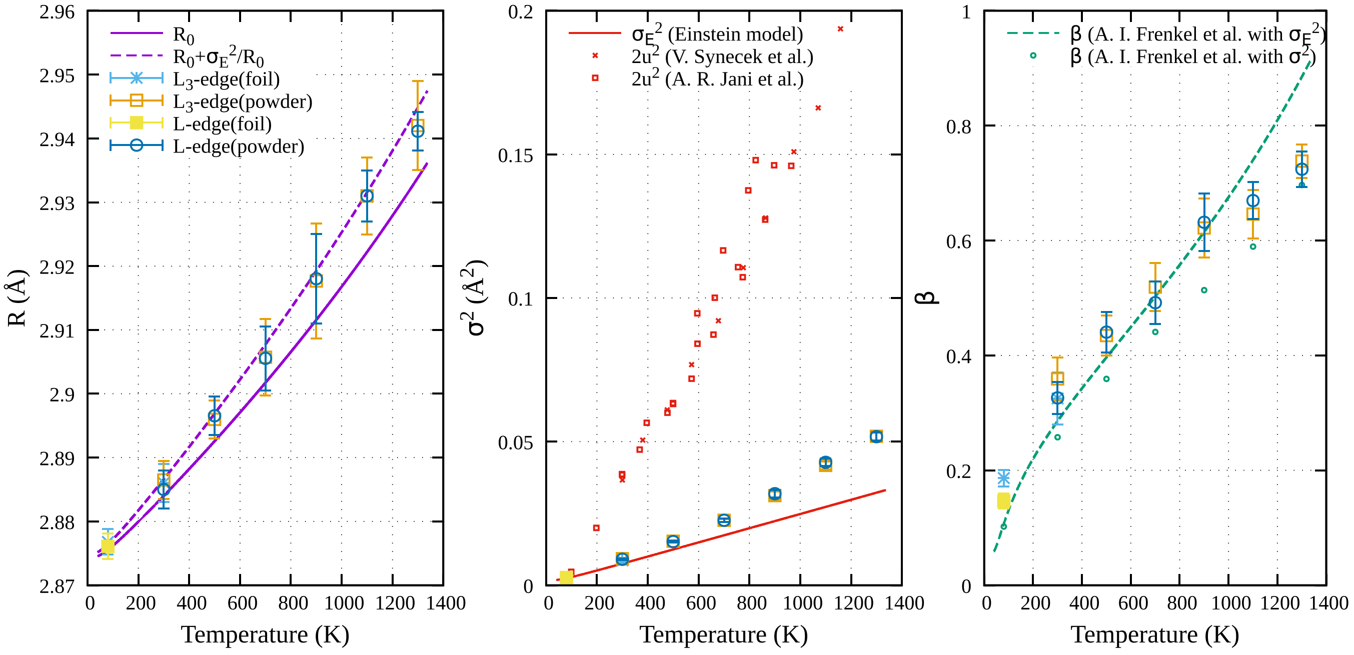

FIG. 4. Structural parameters of the first shell distribution as a function of temperature for solid c-Au obtained by L_3 and multiple L-edge XAFS analysis [blue circle points - multiple L-edge (powder); orange square points - L_3-edge (powder); yellow filled square points - multiple L-edge (foil reference); light blue star points - L_3-edge (foil reference)]. (Left) Comparison of the temperature dependence of the first-neighbor bond length given by the XAFS data analysis, R (points with error bars), with the first-shell equilibrium distance given by XRD [17], $R_0 = a/\sqrt{2}$ (purple solid line), and with the estimate accounting for correlated vibrations, $R_0 + \sigma^2/R_0$ [see Eq. (5)] [34,35], σ^2 being the bond variance. Middle panel: comparison of the first-neighbor bond variance given by XAFS, σ^2 (points with error bars), with the simple correlated Einstein model [see Eq. (6); red continuous line] [36], and with the uncorrelated experimental XRD estimates given by twice the mean-square displacement, $2\langle u^2\rangle$ (red stars and red squares for the works of respectively Refs. [37] and [38]). (Right) Comparison of the temperature dependence of the first-neighbor bond asymmetry parameter given by XAFS, β (points with error bars), with the estimation based on Ref. [39] for the third cumulant of the vibrational amplitude, C_3/σ^3 [see Eq. (7), green dashed line calculated using Einstein model variance σ_E^2 and green circle using σ^2 from our analysis], σ^2 being the XAFS bond variance.

reported in Fig. 5, there are strong positive correlations among the chosen parameters (R and E_0, as well as R and β).

C. Liquid Au

Elemental Au melting occurring at $T_m = 1337$ K [17] is clearly displayed by our L-edge XAFS data as a discontinuous change involving a rounding of the near-edge structures and a shape/phase shift of the $\chi(k)$ signal. This effect can be appreciated looking at Fig. 6 where we compare the $k\chi(k)$ signals of crystalline Au (at $T = 1300$ K, below T_m) and liquid Au (at $T = 1400$ K, above T_m). The two XAFS signals show a

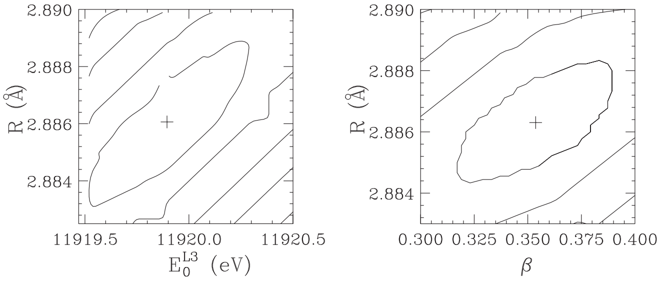

FIG. 5. Contour maps of the residual function for powder c-Au L_3-edge XAFS at 300 K. (Left) Contour map for E_0 and R (first-neighbor distance) parameter. The first ellipsoid include the acceptable E_0 and R values corresponding to 95% confidence level (error of about 0.003 Å on R in this case). (Right) Contour map for the first-neighbor asymmetry parameter β and distance R.

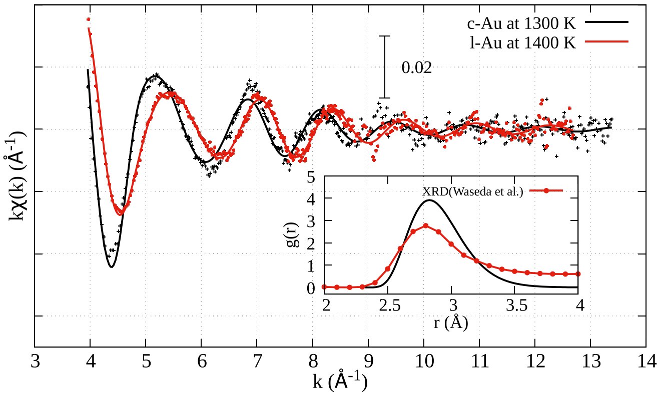

FIG. 6. Comparison between the experimental (dots) and calculated (solid lines) $k\chi(k)$ L_3-edge XAFS signal of solid (c-Au, $T = 1300$ K, black color) and liquid ($T = 1400$ K, red color) Au, obtained using multiple-edge best-fit procedures described in the text. The $g(r)$ pair distribution functions of solid Au (derived from present XAFS data) and liquid Au (obtained by XRD [15]) are also shown in the inset.

distinct change in phase indicating that the effective frequency of the XAFS signal is slightly lower in the liquid phase.

Present knowledge about the structure of liquid Au (l-Au) arises from the measurement of the pair distribution function [$g(r)$] by Waseda [15,16], that has been obtained by Fourier transform of the x-ray diffraction structure factor $S(Q)$, where Q is the scattering vector, at the temperature of 1423 K (the corresponding atomic density being 0.0525 atoms/Å^3);

$$g(r) = 1 + \frac{1}{2\pi^2 r\rho}\int_0^\infty Q[S(Q) - 1]\sin(Qr)\,dQ \qquad (2)$$

and $S(Q)$ is calculated from measured total intensity normalised by number of atoms with atomic scattering factor. Detail of liquid $g(r)$ were written in Ref. [15,16]. It is quite interesting to note that while the density decreases by about 6% upon melting, the position of the first-neighbor peak of the $g(r)$ is found slightly shifted to shorter distances. This can be appreciated looking at the inset of Fig. 6, where we compare the reconstructed first-shell $g(r)$ of c-Au at 1300 K with that of l-Au at 1423 K (XRD [15,16]). In this figure, the pair distribution function g(r) of c-Au is obtained as

$$g(r) = \frac{Np(r)}{4\pi\rho r^2}, \qquad (3)$$

where N is the coordination number (N=12 for f.c.c. structure), $\rho = 4/a^3$ is the density (atoms/Å^3) obtained using the lattice constant $a = a(T)$ [17] at T=1300 K, and $p(r)$ is given by Eq. (1) using the parameters of Table I (c-Au at 1300 K). It is worth mentioning that the similar function $G(r) = 4\pi r\rho[g(r) - 1]$, called PDF, is frequently used especially for solid-state systems.

Data-analysis of liquid Au L-edge XAFS spectra has been performed using standard procedures within GNXAS [19,25,40] using multiple-edge refinements [24]. Within these procedures, a robust reconstruction of the pair distribution at short distances is obtained taking into account the asymptotic properties of a model pair distribution function (here measured by XRD [15,16]) and the compressibility limit which result in proper constraints for the structural parameters defining the first peak of the $g(r)$. To this purpose, the model $g(r)$ [15,16] has been decomposed into two short-range peaks in order to get an adequate parametrization of the first-neighbour peak of the pair correlation function. This decomposition has been done by means of two Γ-like functions [25], in the distance range between 2.0 and 3.4 Å, as also reported in other cases [24,41]. The graphical result of the decomposition of the model $g(r)$ is reported in Fig. 7. Best-fit values for the coordination number N, average distance R, variance σ^2, and dimensionless skewness β are reported in Table II (XRD). As described elsewhere [19,25,42], useful constraints for the structural parameters used for XAFS refinements of a monoatomic liquid are

$$\Delta(N_1 + N_2) = 0,$$
$$\Delta\left[N_1\left(R_1^2 + \sigma_1^2\right) + N_2\left(R_2^2 + \sigma_2^2\right)\right] = 0, \qquad (4)$$

which preserve the total coordination number and the correct compressibility limit. In this case those sum-rule constraints are respectively: $N = N_1 + N_2 = 12.356$ and $M^{(2)} = N_1(R_1^2 + \sigma_1^2) + N_2(R_2^2 + \sigma_2^2) = 123.683$.

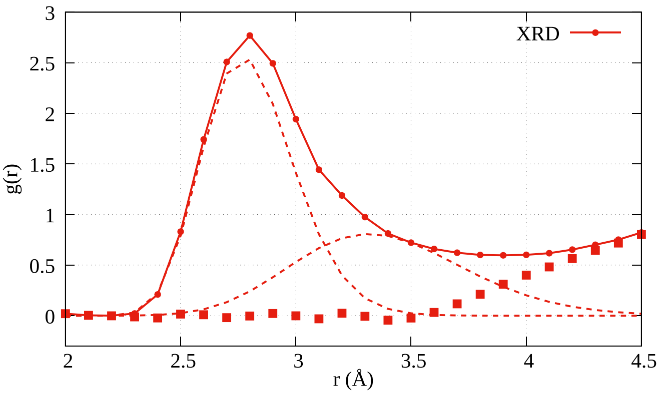

FIG. 7. Decomposition into two Γ-like peaks (dashed lines) and a long-range tail (squares) of the model pair distribution function $g(r)$ as obtained by XRD [15,16] (red dots). The best-fit curve is shown as a red continuous line.

We have thus calculated the irreducible two-body multiple-scattering $\gamma^{(2)}$ signals to be used in the refinement of the XAFS L-edge data of l-Au at 1400 K. Calculations were done using relativistic phase-shifts as described in Sec. III A for both the two Γ-like distributions ($\gamma_1^{(2)}$ and $\gamma_2^{(2)}$ for peaks 1 and 2 respectively) and the long-range tail reported in Fig. 7. The tail contribution was calculated using a maximum cut-off distance of 14.0 Å and a Gaussian window [19] to avoid termination ripples, and resulted to be negligible.

Figure 8 shows a comparison between the experimental and calculated XAFS signal in l-Au at 1400 K. Calculated XAFS signals were evaluated directly from the model pair distribution function (light blue lines) by XRD [15,16] and were subsequently optimized using multiple-edge refinements accounting for the constraints of Eq. (4) (XAFS best-fit signals shown as orange lines). Clearly, the XAFS signals derived directly from the model $g(r)$ are not able to reproduce the experimental XAFS signals. The lower amplitude of the XRD-based signals can be appreciated looking both at the XAFS spectra and Fourier transform in Fig. 8.

Structural refinements of the L-edge XAFS spectra of l-Au were carried out considering the constraints of Eq. (4) and the estimates of the atomic background and nonstructural parameters optimized for the XAFS analysis of c-Au described in the preceding section.

TABLE II. Parameters defining the two Γ-like functions reproducing the first $g(r)$ peak of liquid Au, as derived by XRD data and multiple-edge XAFS data. Typical error bars on first-neighbor distances R_i, variances σ_i^2, and skewness β_i obtained by XAFS are reported in brackets. Coordination numbers are defined by the constraints reported in Eq. (4).

	Peak	N_i	R_i (Å)	σ_i^2 (Å^2)	β_i
XRD [15,16]	1	6.612	2.839	0.0420	0.397
	2	5.744	3.472	0.149	0.365
XAFS L edge	1	4.864	2.816(5)	0.035(3)	0.78(3)
	2	7.492	3.34 (2)	0.16(1)	0.76(9)

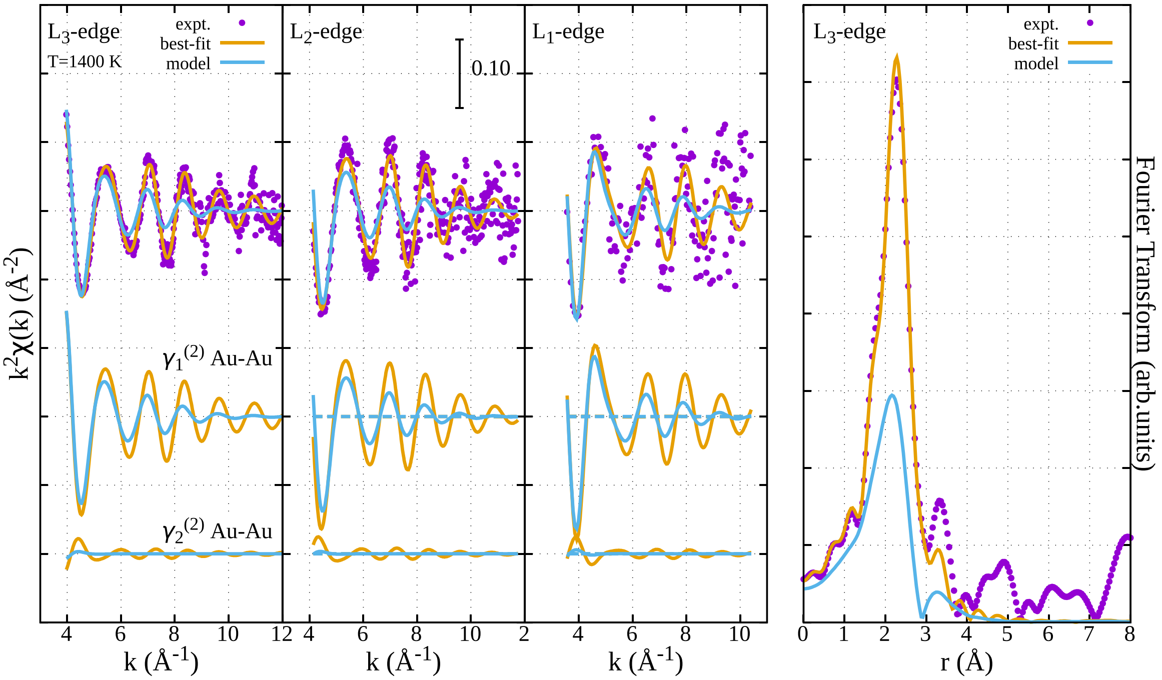

FIG. 8. (Left panels, upper curves) L_3, L_2, and L_1 experimental XAFS $k^2\chi(k)$ data of liquid Au at 1400 K (expt., purple dots) compared with calculations based on the $g(r)$ model (XRD [15,16], light blue) and present multiple-edge refinements (best-fit, orange). (Left panels, lower curves) Individual Au-Au contributions related to the decomposition of the first-neighbor $g(r)$ peak as described in the text (same colors as above). Continuations of the signal of previous edges are reported as dashed lines. (Right) Comparison of the Fourier transforms of L_3 XAFS experimental (purple dots) and calculated (model XRD [15,16], light blue and XAFS best-fit, orange) signals.

The best-fit structural parameters describing the first peak of the $g(r)$ in l-Au are reported in Table II (XAFS L-edge).

Based on this structural refinement, we have reconstructed the short-range $g(r)$ of l-Au, which is shown in Fig. 9 (orange line) as compared with the model $g(r)$ obtained by XRD [15,16] (red dots). We also report in Fig. 9 the error bars evaluated using a suitable statistical analysis of the multiparametric nonlinear fitting procedure. This analysis included correlations between relevant parameters for the present XAFS calculation namely E_0; R_i, σ_i^2, β_i (with $i = 1, 2$ for the two asymmetric peaks of the $g(r)$ decomposition); S_0^2.

Looking at the results of Figs. 8 and 9, we can clearly see that the XAFS signals are extremely sensitive to the shape of the first-neighbor peak of the pair distribution $g(r)$. In particular, the steeper foot of the distribution and the small shift of the first-peak position as compared to the model $g(r)$ are quite accurately measured by XAFS and represent a robust structural refinement that we discuss further in Sec. IV.

IV. DISCUSSION

Our results on crystalline gold should be placed in the context of the present knowledge about the static and dynamical properties of the Au crystal as a function of temperature. Clearly, lattice expansion properties are measured accurately by diffraction experiments so we have reliable information about the evolution of the lattice constant a of the Au f.c.c. lattice (see Ref. [17] and references therein). XAFS experiments probe the pair and high order distribution functions so measuring averages of the interatomic distances which are different quantities as compared to the distance between equilibrium positions related to the lattice constant a.

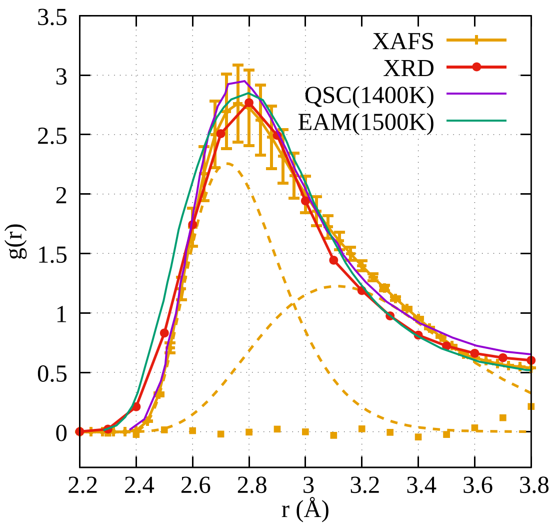

FIG. 9. Reconstruction of the liquid Au (continuous orange line) pair distribution $g(r)$ obtained by XAFS compared with: XRD data [15,16] (red dots), MD simulation with QSC potential [43] (continuous purple line) and with EAM potential [11](continuous green line). The individual contributions to the first $g(r)$ peak reconstructed by XAFS are also shown (orange dashed lines and dots). Estimated error bars on the present XAFS reconstruction allow us to detect differences with previous XRD data and MD models and appears to be in quite good agreement with QSC simulations at short distances.

In particular, the average distance R measured by XAFS results to be slightly longer than the corresponding distance $R_0(a)$ between the atom equilibrium sites in the lattice. This is an effect of the thermal vibrations which also involve distance fluctuations orthogonal to the bond direction, that we can indicate as $\sigma_\perp^2$ [34]. For an isotropic distribution $\sigma_\perp^2 = 2\sigma^2$ [35] where σ^2 is the bond variance:

$$R \sim R_0 + \frac{\sigma_\perp^2}{2R_0} = R_0 + \frac{\sigma^2}{R_0}. \tag{5}$$

The limiting values for the bond variance at any temperature can be estimated by assuming an uncorrelated limit for which σ^2 is just the sum of the mean square displacements of the atom equilibrium positions $\langle u^2\rangle$ usually measured by diffraction techniques (see Refs. [37,38] for Au). Literature values for $2\langle u^2\rangle$ are reported in the middle panel of Fig. 4.

The σ^2 variances of the first-neighbor bonds are much smaller as compared to the limiting $2\langle u^2\rangle$ values, as an effect of the correlated motion of the couples. The trend of the bond variances with temperature can be estimated using a simple Einstein model for vibrations [36]

$$\sigma^2(T) = \frac{\hbar}{\mu\omega_E}\coth\frac{\beta_T\hbar\omega_E}{2}, \tag{6}$$

where $\beta_T = 1/k_B T$ and μ is the reduced atomic mass of the couple. This model is based on the definition of an effective Einstein frequency $\omega_E(\sigma^2)$. A useful approximation [36] was found to be $\omega_E(\sigma^2) \simeq \frac{3}{4}\omega_D$, so related to the Debye frequency $\omega_D = k_B\Theta_D/\hbar$ of the system, where Θ_D is the Debye temperature (Θ_D = 188 K [17] in Au, the present case).

In the left and middle panels of Fig. (4), we compare multiple-edge XAFS results for, respectively, the first-neighbor distance R and variance σ^2 with the relevant data obtained from literature. The first-neighbor average distance R is found to be systematically larger than the corresponding value $R_0 = a/\sqrt{2}$ as expected, and we obtain a reasonable agreement within the errors with the approximation $R_0 + \frac{\sigma^2}{R_0}$ described above. The bond variances σ^2 resulting from XAFS structure refinement reported in the middle panel of Fig. 4 are consistent with the predictions of a simple Einstein model [red solid line, see Eq. (6)] at moderate temperatures below 500 K. At higher temperatures, they depart from this simple model still being much below the uncorrelated limit $2\langle u^2\rangle$ as estimated by diffraction [37,38].

The deviation from a simple Einstein model at high temperature can be understood considering that all phonon modes are activated and deviations from a simple harmonic approximation are gradually larger with temperature. This fact can be appreciated looking also at the trend of the β parameter, measuring the skewness of the bond distribution, for increasing temperatures. In fact, $\beta = 0$ in the harmonic approximation is expected to work fine at low temperatures. This is confirmed by the trend reported in Fig. 4, right-hand panel, where β is found to increase at high temperatures indicating large deviation from a simple Gaussian distribution of distances. The trend is found to be in qualitative agreement with the relationship based on the correlated Einstein model of Ref. [39] between the linear thermal expansion coefficient ($\alpha = \frac{1}{R_0}\frac{dR_0}{dT}$, determined in our case from a numerical derivation of the XRD data of Ref. [17]) and the second and third cumulants of the vibrational amplitude,

$$\beta = \frac{C_3}{\sigma^3} = \frac{\alpha R_0 T}{\sigma}\left(\frac{3z(1+z)\ln(1/z)}{(1-z)(1+10z+z^2)}\right)^{-1}, \tag{7}$$

where $z = e^{-\Theta_E/T}$, with $\Theta_E = \frac{3}{4}\Theta_D$, as mentioned before for Eq. (6); σ^2 is the bond variance as given by the present XAFS data analysis. Systematic deviations of the dimensionless skewness parameter between the correlated Einstein model and the present XAFS data analysis are observed at both low and high temperatures.

A striking change of the L-edge Au XAFS spectra was observed upon melting as it can be appreciated in Fig. 6. This change reflects the important modification in the short-range distribution of distances (see also inset of Fig. 6) and shows how sensitive XAFS can be to phase transitions.

Our current knowledge of the average Au liquid structure was mainly associated with the pair distribution $g(r)$ obtained by high-temperature XRD (x-ray diffraction) experiments [15,16]. As it is well known, XAFS is very sensitive to short-range ordering but it is almost blind to medium and long-range correlations to which XRD is sensitive so the two techniques are highly complementary. We have thus applied a highly-reliable XAFS data-analysis method to refine the first-neighbor $g(r)$ peak of liquid Au at 1400 K for which the results are reported in Figs. 8 and 9. Looking at Fig. 8, it is quite evident that the XAFS signals associated with the model $g(r)$ (obtained by XRD, light blue) is unable to explain present multiple-edge XAFS data (shown in purple). The average amplitude of the model is much lower as also shown by the comparison of the Fourier transforms. Moreover, a slight shift of the frequency in k space is observed.

The XAFS signal is extremely sensitive to the very short-range distances as it can be also appreciated looking at the different amplitudes of the signals associated with the two Γ-like functions reproducing the first peak of the $g(r)$. The peak corresponding to the shortest distances (peak 1 in Table I) gives actually the dominant contribution to all L-edge XAFS spectra. As a consequence, our constrained XAFS refinement of the $g(r)$ of liquid Au, shown in Fig. 9, resulted in variations of the $g(r)$ shape at very short range. In particular, a clear shift of the foot of the distribution to longer distances of about 0.1 Å and a slight shortening of the position of the maximum (from 2.80 to 2.77 Å) is observed. The rise of the first-neighbor distribution is found to be much steeper as compared to that previously obtained by XRD. This behavior is similar to that of solid g(r) at high temperatures, as shown in Fig. 6. Comparing with MD calculation, EAM-based Quantum Sutton-Chen(QSC) potential [43] shows better agreement with our $g(r)$ than other interatomic potential models [9–11]. The XAFS L-edge spectra are extremely sensitive to these details of the distribution as can be appreciated looking at the quality of the best-fit refinement shown in Fig. 8.

V. CONCLUSIONS

In this work, we investigated the local structure of solid and liquid gold using L_i-edge ($i = 1$, 2, and 3) multiple-edge XAFS refinements in the temperature range 80-1400 K. High-quality data at high temperatures in solid and liquid phase were obtained producing suitable gold samples as a dispersion of submicrometric Au particles, by *in situ* reduction of an organic precursor.

XAFS data-analysis was carried out using reliable multiple-scattering calculations including relativistic corrections (GnXAS), especially important for heavy elements like Au. Multiple L_i-edge ($i = 1, 2,$ and 3) XAFS refinements were performed using suitable procedures including proper background functions incorporating double-electron contributions.

Results concerning the local structure were compared with present knowledge related to previous studies based mainly on x-ray diffraction data. In the solid phase, we have studied the trend of the first-neighbor structural parameters in a wide temperature range 80–1300 K. The average first-neighbor distance was observed to increase with temperature and results were found to be compatible with the known thermal expansion and with the effect of vibrations orthogonal to the bond direction. The bond variance (or mean-square relative displacement) σ^2 was also found to increase with temperature, departing from a simple Einstein model at high temperatures (above 500 K). An increased asymmetry of the first-neighbor distribution was observed for increasing temperatures showing clearly the effect of anharmonic vibrations. A detailed error analysis including correlations among fitting parameters was performed to assess the accuracy of our results.

Refinement of the average structure of liquid Au at 1400 K has been carried out considering the short-range contribution to the pair distribution function $g(r)$, using present x-ray diffraction data [15,16] as a constraint for long-range order within well established procedures for XAFS data-analysis of liquids [19].

We have shown that XAFS is extremely sensitive to the first-neighbor distribution and that the $g(r)$ is characterized by a shift of the foot of the distribution to longer distances (∼0.1 Å) and by a slight shortening of the position of the maximum (from 2.80 to 2.77 Å), with a much steeper rise of the first-neighbor $g(r)$ peak, as compared to previous experimental results. The XAFS sensitivity to local structure was found to be very high and present data are thought to be very accurate, improving present knowledge of the structure in liquid Au. In particular, the shape of the first $g(r)$ peak is strongly related to the model of the repulsive interatomic potential used in typical MD simulations so we were able to test the validity of different potential models. In general, the improvement in structure knowledge obtained in this work poses constraints to theoretical and computer simulation works attempting to develop reliable model interactions able to describe elemental Au in a wide temperature range.

ACKNOWLEDGMENTS

The authors kindly acknowledge funding by PNRR MUR Project No. PE0000023-NQSTI.

[1] R. Briggs, F. Coppari, M. G. Gorman, R. F. Smith, S. J. Tracy, A. L. Coleman, A. Fernandez-Pañella, M. Millot, J. H. Eggert, and D. E. Fratanduono, Phys. Rev. Lett. **123**, 045701 (2019).

[2] S. M. Sharma, S. J. Turneaure, J. M. Winey, Y. Li, P. Rigg, A. Schuman, N. Sinclair, Y. Toyoda, X. Wang, N. Weir, J. Zhang, and Y. M. Gupta, Phys. Rev. Lett. **123**, 045702 (2019).

[3] G. Weck, V. Recoules, J.-A. Queyroux, F. Datchi, J. Bouchet, S. Ninet, G. Garbarino, M. Mezouar, and P. Loubeyre, Phys. Rev. B **101**, 014106 (2020).

[4] T. A. Assefa, Y. Cao, S. Banerjee, S. Kim, D. Kim, H. Lee, S. Kim, J. H. Lee, S.-Y. Park, I. Eom, J. Park, D. Nam, S. Kim, S. H. Chun, H. Hyun, K. sook Kim, P. Juhas, E. S. Bozin, M. Lu, C. Song *et al.*, Sci. Adv. **6**, eaax2445 (2020).

[5] H. Häkkinen, Chem. Soc. Rev. **37**, 1847 (2008).

[6] Q. Li, W. Niu, X. Liu, Y. Chen, X. Wu, X. Wen, Z. Wang, H. Zhang, and Z. Quan, J. Am. Chem. Soc. **140**, 15783 (2018).

[7] S. Van Petegem, S. Brandstetter, R. Maass, A. M. Hodge, B. S. El-Dasher, J. Biener, B. Schmitt, C. Borca, and H. Van Swygenhoven, Nano Lett. **9**, 1158 (2009).

[8] L. F. Pašteka, E. Eliav, A. Borschevsky, U. Kaldor, and P. Schwerdtfeger, Phys. Rev. Lett. **118**, 023002 (2017).

[9] F. Kirchhoff, M. J. Mehl, N. I. Papanicolaou, D. A. Papaconstantopoulos, and F. S. Khan, Phys. Rev. B **63**, 195101 (2001).

[10] G. Grochola, S. P. Russo, and I. K. Snook, J. Chem. Phys. **123**, 204719 (2005).

[11] H. W. Sheng, M. J. Kramer, A. Cadien, T. Fujita, and M. W. Chen, Phys. Rev. B **83**, 134118 (2011).

[12] M. Backman, N. Juslin, and K. Nordlund, Eur. Phys. J. B **85**, 317 (2012).

[13] Z.-L. Liu, Y.-P. Tao, X.-L. Zhang, and L.-C. Cai, Comput. Mater. Sci. **114**, 72 (2016).

[14] M. Wu, J. Shi, Y. Wu, Y. Ma, and Z. Ding, AIP Adv. **10**, 045038 (2020).

[15] Y. Waseda, *The Structure of Non-Crystalline Materials* (McGraw-Hill, New York, 1980).

[16] Y. Waseda and M. Ohtani, phys. stat. sol. (b) **62**, 535 (1974).

[17] M. G. Pamato, I. G. Wood, D. P. Dobson, S. A. Hunt, and L. Vočadlo, J. Appl. Crystallogr. **51**, 470 (2018).

[18] J. J. Rehr and R. C. Albers, Rev. Mod. Phys. **72**, 621 (2000).

[19] A. Filipponi, J. Phys.: Condens. Matter **13**, R23 (2001).

[20] A. Filipponi, A. Di Cicco, and C. R. Natoli, Phys. Rev. B **52**, 15122 (1995).

[21] G. Tchoudinov, A. Di Cicco, and C. R. Natoli, Phys. Rev. B **105**, 144109 (2022).

[22] A. Filipponi and A. Di Cicco, Phys. Rev. B **52**, 15135 (1995).

[23] N. Hara, A. Di Cicco, G. Tchoudinov, K. Hatada, and C. R. Natoli, Symmetry **13**, 1021 (2021).

[24] A. Di Cicco, Phys. Rev. B **53**, 6174 (1996).

[25] A. Filipponi and A. Di Cicco, Phys. Rev. B **51**, 12322 (1995).

[26] T. Comaschi, A. Balerna, and S. Mobilio, Phys. Rev. B **77**, 075432 (2008).

[27] M. A. Karolewski, R. G. Cavell, R. A. Gordon, C. J. Glover, M. Cheah, and M. C. Ridgway, J. Synchrotron Radiat. **20**, 555 (2013).

[28] A. Filipponi and A. Di Cicco, Nucl. Instr. Meth. B **93**, 302 (1994).

[29] L. Ottaviano, A. Filipponi, and A. Di Cicco, Phys. Rev. B **49**, 11749 (1994).

[30] A. Di Cicco, M. Taglienti, M. Minicucci, and A. Filipponi, Phys. Rev. B **62**, 12001 (2000).

[31] T. Yokoyama, Microstructures **1**, 2021003 (2021).

[32] R. E. Benfield, A. Filipponi, D. T. Bowron, R. J. Newport, and S. J. Gurman, J. Phys.: Condens. Matter **6**, 8429 (1994).

[33] A. Di Cicco and A. Filipponi, Phys. Rev. B **49**, 12564 (1994).

[34] F. D. Vila, J. J. Rehr, H. H. Rossner, and H. J. Krappe, Phys. Rev. B **76**, 014301 (2007).

[35] A. Sanson, J. Synchrotron Radiat. **15**, 514 (2008).

[36] E. Sevillano, H. Meuth, and J. J. Rehr, Phys. Rev. B **20**, 4908 (1979).

[37] V. Syneček, H. Chessin, and M. Simerska, Acta Crystallographica Section A **26**, 108 (1970).

[38] A. R. Jani and V. B. Gohel, Zeitschrift für Naturforschung A **38**, 503 (1983).

[39] A. I. Frenkel and J. J. Rehr, Phys. Rev. B **48**, 585 (1993).

[40] A. Filipponi, J. Phys.: Condens. Matter **6**, 8415 (1994).

[41] J. Dziedzic and J. Rybicki, J. Non-Cryst. Solids **354**, 4316 (2008), functional and Nanostructured Materials.

[42] A. Trapananti and A. Di Cicco, Phys. Rev. B **70**, 014101 (2004).

[43] Ü. Domekeli, S. Sengul, and M. Celtek, in *International Scientific Conference "UNITECH 2022" – Gabrovo* (2022), pp. II–345.